

Nanoscale

Accepted Manuscript



This is an *Accepted Manuscript*, which has been through the Royal Society of Chemistry peer review process and has been accepted for publication.

Accepted Manuscripts are published online shortly after acceptance, before technical editing, formatting and proof reading. Using this free service, authors can make their results available to the community, in citable form, before we publish the edited article. We will replace this *Accepted Manuscript* with the edited and formatted *Advance Article* as soon as it is available.

You can find more information about *Accepted Manuscripts* in the [Information for Authors](#).

Please note that technical editing may introduce minor changes to the text and/or graphics, which may alter content. The journal's standard [Terms & Conditions](#) and the [Ethical guidelines](#) still apply. In no event shall the Royal Society of Chemistry be held responsible for any errors or omissions in this *Accepted Manuscript* or any consequences arising from the use of any information it contains.

Nanodiamonds from coal at ambient conditions

J. Xiao, P. Liu, G. W. Yang[†]

State Key Laboratory of Optoelectronic Materials and Technologies, Nanotechnology

Research Center, School of Physics & Engineering, Sun Yat-sen University,

Guangzhou 510275, Guangdong, P. R. China

[†] Corresponding author: stsygw@mail.sysu.edu.cn

Abstract

Coal is the most abundant energy resource, but it is only useful for producing energy via combustion due to its structural characteristics. However, coal is also inexpensive and is the most plentiful and readily available carbon source material for the production of nanodiamonds compared with the most widely used solid carbon source, high-purity graphite, and the high-purity hydrocarbon gas precursor, methane. Here, we report a simple and green top-down strategy for synthesizing nanodiamonds with a cubic phase and a mean size of 3 nm from various types of coal at atmospheric pressure and room temperature using a novel process involving laser ablation in liquid. Furthermore, we have systematically studied the process of phase transformation from coal to nanodiamonds by means of nucleation thermodynamics, growth kinetics and structural stability. The synthesized nanodiamonds are turns out to be soluble monodisperse colloids that exhibit strong and stable fluorescence both in alcohol and water. These results provide a route for producing nanodiamonds from inexpensive and abundant coal.

Keywords: nanodiamonds, coal, laser ablation in liquid

1. Introduction

Coal is the most abundant energy resource, and it is used for producing energy worldwide via combustion¹. As a molecular solid, coal has a complex structure²⁻⁵. The crystalline carbon within the coal structure consists of abundant irregular, polymerized aromatic hydrocarbon units, such as angstrom- or nanometer-sized crystalline carbon domains that are joined by weak cross-links^{6,7}. Compared with crystalline carbon allotropes, so-called lattice solids, such as graphite and diamond that have found applications in areas such as microelectronics, optoelectronics and biomedicine^{8,9}, coal is mainly used as a combustible energy resource due to its structural characteristics.

Because coal is an inexpensive and readily available source of carbon, it is naturally interesting to explore the synthesis of diamonds directly from coal to reduce the production costs. Nanodiamonds have been synthesized for research using the detonation technique¹⁰, laser ablation¹¹, plasma-assisted chemical vapor deposition (CVD)¹² and other techniques¹³⁻¹⁸, with the first two of these methods being used commercially⁹. However, value-added sources of carbon, such as graphite and high-purity hydrocarbon gas, have been widely used in the aforementioned nanodiamonds production techniques. Additionally, producing nanodiamonds with sizes smaller than 4 nm and de-aggregating colloidal solutions have remained challenging⁹.

Here, we report a simple and environmentally friendly top-down strategy for synthesizing nanodiamonds from three types of coal under ambient conditions using a

novel process of laser ablation in liquid. The synthesized nanodiamonds particles possess a cubic structure and a mean size of 3 nm. Furthermore, the synthesized nanodiamonds are soluble monodisperse colloids in aqueous solution and show strong and stable photoluminescence (PL), which provides them with considerable potential in the fields of biomedical imaging, photovoltaics and optoelectronics.

2. Experimental

The raw anthracite (Vietnam), bitumite (Indonesia) and coke (China) coals are ultrasonically cleaned with water and absolute alcohol three times to remove adsorbed impurities and organic pollutants. The details of the laser ablation in liquid procedures have been reported in our previous publications^{19,20}. Here, approximately 5 mg of raw coal was placed in a 10 mL bottle filled with absolute alcohol. Then, the second harmonic produced by a Q-switched Nd:YAG laser device with a wavelength of 532 nm, a pulse width of 10 ns, a repetition frequency of 10 Hz and a laser-pulse energy of 200 mJ was focused on the middle of the bottle. The spot size was 1 mm, and the samples were ablated for different intervals. The whole experiment lasts for 2h. The C₂ emission spectrum was obtained using an intensified charge-coupled device (ICCD) (Andor, New ISTAR ICCD) as a detector. The emission is firstly collected by an optical receiver, and then it is transferred into grating spectrometer by means of fiber optic cable. This signal is continued to guide into CCD and finally get the spectra. In order to enhance the signal-noise ratio, we collect the signal by accumulating 20 times. The duration of the gate was set to 30 ns, and the time delay after the laser pulse was

100ns. The measurement was mainly performed in the range from 500 to 570 nm, in which the $\Delta v = -1, 0$ band of the Swan system of C_2 molecules are observed.

After the ablation, one drop of the solution was pipetted onto a carbon support film on a copper grid for transmission electron microscopy (TEM) observation. TEM and high-resolution TEM (HRTEM) images were recorded using an FEI Tecnai G2 F30 transmission electron microscope equipped with a field-emission gun. X-ray diffraction (XRD) patterns were recorded on a Rigaku D/Max-III A X-ray diffractometer with Cu K α radiation ($\lambda = 1.54056 \text{ \AA}$, 40 kV, 20 mA) at a scan rate of 1° s^{-1} . Raman spectra were recorded on a Renishaw inVia Plus laser micro-Raman spectrometer using Ar ion laser irradiation of $\lambda = 325 \text{ nm}$. XPS (ESCALab250) was employed to analyze the composition of the surface of samples. Fourier transform infrared spectroscopy (FTIR) was performed using a Bruker EQUINOX55. PL spectrum measurements were performed using an Edinburgh spectrofluorophotometer (FLS920) at room temperature with a 450 W xenon lamp and with a photomultiplier tube as a detector operating in the photon-counting mode.

3. Results and Discussion

As shown in Figure 1a-b, ground anthracite coal clearly consists of rugged and jagged micro-sized particles with irregular sizes and shape distributions. The other coals, including bitumite and coke, have similar shapes (Supplementary Figure S1a and Figure S1d). The energy dispersive X-ray spectroscopy (EDS) analysis indicates that anthracite and coke contain pure carbon without any other impurities but that

bitumite contains oxygen in addition to carbon (Supplementary Figure S1c). These micro coal particles serve as the raw materials in our study. The experiments are performed using the process of laser ablation in liquid^{19,20} (the detailed experimental process is presented in the experimental section). After ablation, the nanodiamonds are synthesized (Figure 1c-h), and they are unagglomerated, uniformly sized and crystalline; in particular, the nanodiamonds have an average diameter that is significantly smaller than 3.1nm, as shown in Figure 1c. Additionally, the sizes of the nanodiamonds obtained from the bitumite and coke coals are 3.6 and 3.2nm, respectively (Supplementary Figure S2 and S3). The corresponding selected area electron diffraction (SAED) (Figure 1d) pattern shows three strong rings that correspond to the (111), (200) and (311) planes of diamonds. The corresponding EDS spectrum (Figure 1e) shows that the nanodiamonds are more oxidized than the original raw coal, which may result from the oxidized groups adsorbed on the surface. The detailed HRTEM image (Figure 1f) shows that the synthesized nanodiamonds can be indexed to the cubic phase of a diamond. Abundant crystalline nanodiamonds can be readily observed in the products (Supplementary Figure S4a). In addition, the (111) twinning plane of the diamond (Figure 1g-h) is observed in the products, which is often the case for cubic diamonds²¹.

The corresponding XRD patterns (Figure 2a) of the products further confirm that the nanodiamonds are synthesized from raw anthracite. The XRD pattern of the raw material only shows a broad peak at approximately 26°, which indicates that the coal consists of abundant amorphous carbon. In comparison, the XRD pattern of the

sample exhibits a peak located at 44° that can be assigned to the (111) lattice plane of a cubic diamond, which is consistent with the SAED results. Although the XRD pattern of the sample exhibits an amorphous carbon signal near 26° , this peak can be attributed to some nanodiamonds embedded within amorphous carbon matrix and some organic groups adsorbed on surface, which is experimentally verified (Supplementary Figure S4b and Figure 6).

Raman spectroscopy is recognized to be one of the most effective techniques for distinguishing sp^3 carbon from sp^2 carbon. Moreover, ultraviolet (UV) excitation (325nm) is used to enhance the scattering from the sp^3 fraction in the sample²². For raw coal, there are two main features in its scattering signal (Figure 2b). The two peaks located at 1382 and 1598 cm^{-1} are close to the positions of the G-band and D-band for sp^2 carbon. However, the Raman spectra of the samples show that the peak at 1325 cm^{-1} exhibits a clear downshift from 1382 cm^{-1} and becomes narrower. Furthermore, the other peak is up-shifted to approximately 1650 cm^{-1} . The value of 1325 cm^{-1} is similar to the well-known Raman scattering peak for bulk diamond at 1332 cm^{-1} . The difference between these two values could be attributed to the phonon confinement effect. According to the Osswald-Mochalin refined phonon-confinement model²³, if the particle diameter is approximately 3nm, the peak position is estimated to appear at $\sim 1323\text{ cm}^{-1}$, which is consistent with our Raman results and TEM observations. In addition, the upshifting of the G band corresponds to the presence of O-H surface functional groups, which can be validated by the above analysis⁹.

Figure 2c presents a comparison of the C1s signals of raw coal and the sample

using X-ray photoelectron spectroscopy (XPS). The anthracite peaks (black squares in top graph) are fit with a Lorentz-Gauss algorithm after a Shirley background subtraction. The peak is located at 284.3eV, which is due to sp^2 -hybridized carbon, whereas the peak at 285 eV has also been added and is attributed to sp^3 -hybridized carbon. The nanodiamonds (red squares in bottom graph) are fit using the same method. The first component of the sample is observed at 284.3eV, which corresponds to sp^2 carbon atoms, and the second component is observed at 285 eV, which corresponds to sp^3 carbon atoms²⁴. A third peak at 286.5eV is attributed to some C-O bond formation, as well as C=O at 288.7eV²⁵. The binding energy values found for the sp^2 and sp^3 components of the nanodiamonds in the C1s spectra are in agreement with the binding energies of 284.4 and 285.2eV detected for the C1s peaks of pure graphite and diamond, respectively²⁴.

In addition, we calculate the change of sp^3 content to estimate the yield of the synthesized nanodiamonds in our case. Before ablation, the sp^3 carbon content in the raw coal is 26.6% (the top graph in Figure 2c), which means that the raw coal have mixed domains with the sp^3 and sp^2 hybridization. However, after ablation, the ratio increases substantially to 54.4% (the bottom graph in Figure 2c). All the content of the raw coal and nanodiamonds have been listed in the table 1. The sp^3 ratio is measured to be the percentage of sp^3 area. The increase of sp^3 content should be partly ascribed to the generation of nanodiamonds. Considering the else amorphous carbon possessing the sp^3 component, the yield of the synthesized nanodiamonds is estimated to be 5-10% in our case. Considering the amount of raw coal and experimental time,

the yield of product in time is estimated to be 0.125-0.25mg/h. Although the XPS method is one of the reliable methods to distinguish sp^3 component from sp^2 component²⁶, as mentioned above, the amorphous carbon or other carbon constituent also possess sp^3 component. Therefore, it is still inaccurate to define what amount the nanodiamonds we get. For this reason, we use a well-accepted method to deal with samples, i.e. high temperature acid treatment²⁷. In order to obtain convincing result, we have to accumulate the samples by repeating experiments. The total samples we synthesize are weighted to be 52.15 mg, and then these samples are dispersed in a mixture of sulfuric acid (98%) and nitric acid (70%; 3:1 v/v, 60mL). The mixture is heated at reflux (90°C) and stirred by a magnetic stirring rotor. During the acid purification, the acid solution became dark brown and send out the yellow smoke. The acid treatment lasts for 5h. After that, the purified samples are centrifuged and washed with deionized water for several times. Finally, the purified samples are dried at 80°C for 24h. It turns out that the weight of purified samples is measured to be 3.23 mg. Besides, we take the XRD characterization of purified sample, as shown in Supplementary Figure S5. Although the amorphous halo still exists, it is getting much weaker and the sign of nanodiamonds is more obvious than that of specimen before the acid treatment (bottom graph in Figure 2a). Generally, the phenomenon that the nanodiamonds contained with some amorphous carbon is common, even in commercial nanodiamonds²⁸. Therefore, the yield of nanodiamonds can be measured to be 6.2%. This percentage composition is close to the reported literature when using high purity graphite as the target instead^{29,30}. We believe by controlling the laser

parameter more detailed, such as wavelength, energy density and ablation time, especially the pulse width, the yield can reach higher.

Therefore, all of these relevant experimental characterizations of the products demonstrate that nanodiamonds with a cubic phase and an average diameter of 3.1nm have been synthesized from coal using the process of laser ablation in liquid.

We now focus the discussion on the formation of nanodiamonds from coal using the process of laser ablation in liquid. During laser irradiation, we can clearly observe a series of significant color changes of the colloid from opaque grayish to dark reddish brown and finally to a transparent yellow (Supplementary Figure S6), indicating the formation of various types of products. We carefully examine the products at the different laser irradiation stages and find an intermediate product during the process of converting coal to nanodiamonds (Figure 3) (taken from the 5th bottle in Supplementary Figure S6). It is clear that the sample exhibits an intersecting and overlapping network (Figure 3a-b). The corresponding SAED pattern confirms that amorphous carbon dominates the sample. Sequentially, the networks fracture into small pieces (Figure 3c-d), similar to the shape of a necklace (taken from the 7th bottle in Supplementary Figure S6). Finally, the linkages disappear, and the small fragments break into many amorphous carbon particles (Figure 3e-f) (taken from the 8th bottle in Supplementary Figure S6). Accordingly, these amorphous carbon particles as an intermediate phase are finally transformed into nanodiamonds by laser ablation in liquid²⁰.

Distinctly, the thermodynamic and kinetic aspects of the laser ablation of coals in

alcohol can greatly influence the phase transformation from raw coals to nanodiamonds. We thus contribute a basic description of the thermodynamic and kinetic factors of the laser ablation of solids in liquid for producing nanodiamonds as follows.

The nucleation thermodynamics. Generally, laser ablation in liquid (LAL) is a rapid process that proceeds under far-from-equilibrium conditions such that all stable and metastable phases that form during the initial, intermediate and final stages of laser ablation remain present in the final products²⁰. In the initial stage of LAL, a large number of carbon reactive species with large initial kinetic energies are ejected from the coal and form a dense region, i.e., a laser-induced plasma plume, in the vicinity of the solid–liquid interface because of the confinement effect of the liquid. Because the plasma plume is strongly confined in the liquid, a shock wave is created with a supersonic velocity at the wavefront, which induces additional pressure, called the laser-induced pressure, in the plasma plume. Furthermore, the laser-induced pressure leads to a temperature increase in the plasma plume. Thus, the plasma plume is driven into a state of the higher-temperature, the higher pressure and the higher density. Subsequently, rapid quenching of the plasma plume will lead to phase formation. As a result of the strong confinement effect of the liquid, the quenching time of the plasma plume in the liquid becomes so short that the metastable phase that forms during the intermediate stage is frozen in the final product. Therefore, LAL is involved in the high temperature and high pressure (HTHP) process, which can reach up to 4000-5000K and 10-15GPa²⁰. We have done a lot of investigations on the

formation of nanodiamonds by the pulsed-laser ablating a graphite target in liquid theoretically and experimentally, and we found out that the nanodiamonds formation upon this process is from the condensation of the laser-induced plasma generated at the liquid-solid interface³¹⁻³³. Although the coal structure are different from the graphite, however, we still believe nucleation mechanism for coal to nanodiamonds is likely to be more physical in nature, such as generating in conventional high-temperature and high-pressure environment. In order to quantitatively analyze the nucleation thermodynamics, we propose a nanothermodynamical model to elucidate the nucleation and the phase transition of nanodiamonds by taking the surface tension induced by the nanosized curvature of crystalline nuclei into account. Firstly, we discuss the real influence of the additional pressure on the stability of diamond phase. Under the assumption of spherical and isotropic nanocrystalline diamond, the size-induced additional pressure $\Delta P=2\gamma/r$, where $\gamma=3.7\text{J/m}^2$ is the surface energy of diamond³³. The size r dependence of additional pressure ΔP is shown in Figure 4a. One can see that additional pressure increase as the particles size decreases, especially when the radius of diamond size is less than 4nm. Due to the additional pressure ΔP that is necessary for the transition from coal to nanodiamonds will decrease by the same amount. Thus, one can obtain the size-dependent equilibrium phase boundary³³

$$P^e = 2.01 \times 10^6 T + 2.02 \times 10^9 T - 2\gamma / r \quad (1)$$

When the conditions are on the equilibrium line given by Eq. (1), we can attain the mole volume Gibbs free energy difference of coal to nanodiamonds transition $\Delta g_{T,P} =$

$\Delta V(P-2.01 \times 10^6 T - 2.02 \times 10^9 T + 2\gamma/r)$. Note that, as coal possess complex constituent, most of them are amorphous carbon, which lack of corresponding phase diagram. In this case, equilibrium phase boundary line is referred to the BS line in graphite-diamond phase diagram. Considering the nanosize effect, the Gibbs free energy difference of the phase transition is³⁴

$$\Delta G(r) = \frac{4}{3} \pi^3 \Delta V (P - 2.01 \times 10^6 T - 2.02 \times 10^9 T + 2\gamma/r) / V_m + 4\pi r^2 \gamma \quad (2)$$

When $\frac{\partial G(r)}{\partial r} = 0$, the critical size of nanodiamonds nuclei is obtained as

$$r^* = 2\gamma \left(\frac{2}{3} + \frac{V_m}{\Delta V} \right) / (2.01 \times 10^6 T + 2.02 \times 10^9 - P) \quad (3)$$

ΔV and V_m are $1.77 \times 10^{-6} \text{ m}^3/\text{mol}$ and $3.417 \times 10^{-6} \text{ m}^3/\text{mol}$, donating molar volume difference between graphite and diamond and molar volume of diamond³⁵. The

dependence of radius r of nanodiamonds critical nucleation on pressure is shown in Figure 4b, If we take the 4000K, 15Gpa, the environment created by LAL, into the curve, we can see that the size of critical size is about 4nm, which is similar to our observation. We can see that even if the graphite parameter is introduced, there is no obvious deviation in the judgment of tendency. Therefore, the usage of graphite-nanodiamonds phase diagram is reasonable. Then, substituting Eq.(3) into Eq.

(2), the critical energy of nanodiamonds nuclei is given as

$$\Delta G(r^*) = \frac{4}{3} \pi r^{*3} \Delta V (P - 2.01 \times 10^6 T - 2.02 \times 10^9 T + 2\gamma/r^*) / V_m + 4\pi r^{*2} \gamma \quad (4)$$

Clearly, one can see that in Figure 4c that the energy of formation of nanodiamonds nuclei increases with increasing temperature at a given pressure. Besides, it indicates that the nucleation of nanodiamonds upon LAL does not need high forming energy, which means that the nucleation is in favor of LAL region.

The probability of phase transformation relate to the activation energy ($E_a - \Delta g_{T,P}$). The general expression of the probability f of the phase transformation from the initial state to the final state is³⁶

$$f = \exp[-(E_a - \Delta g_{T,P}) / RT] - \exp[-(E_a / RT)] \quad (5)$$

Where R is the gas constant, 8.31J/kmol, E_a is the maximum potential energy for both sides with respect to the general coordinate, 120kJ/mol. The P-T curve with radius $r=3\text{nm}$ are shown in Figure 4d. It shows that the probability of the phase transition is high, which can reach up to 10^{-3} - 10^{-2} in the pressure range of 10-15 Gpa and the temperature range of 4000-5000K (backslash pattern in Figure 4d).

Note that, the conversion possibility is not the same concept as the yield of nanodiamonds. The conversion possibility indeed is associated with the yield. However, it is not the simple linear dependence relationship. For example, the detonation method is well known approach to synthesize a large amount of nanodiamonds. Using this method, the yield of nanodiamonds can reach 40-90%³⁷. However, in our diagram, the conversion possibility are shown to be a little smaller than 10^{-2} (orthogonal grid pattern in Figure 4d) due to the reaction environment in the pressure range of 10-16.5 GPa and the temperature range of 2900-3900K³⁸, which is slightly smaller than that using LAL method. The reason that conversion rate and yield exist such significant difference is that in terms of detonation method, the nanodiamonds yield after detonation crucially depends on the synthesis condition and especially on the heat capacity of the cooling medium in the detonation chamber (water, air, CO₂, etc.) The higher the cooling capacity, the larger the nanodiamonds

yield, which can reach 90%²⁸. Thus, in our case, the conversion possibility only points out the “probability” that transformation from coal to nanodiamonds, however, the practical yield should depend on the synthesis parameter, such as laser wavelength, energy density, pulse width and the used liquid.

The growth kinetics. Structurally, coal is a macromolecular solid that consists of abundant irregular, polymerized aromatic hydrocarbon units that are joined by weak links. In other words, organic material dominates, typically representing 85-95% (wt/wt) of dry coal⁴. Therefore, in the case of the coal-derived carbon, the phase transformation significantly differs from that of graphite because of the striking difference in their textures. The transition from graphite to diamond occurs during the process of the HTHP-driven phase transformation from hexagonal to cubic carbon. Yang *et al.* suggest that the diamond transition from hexagonal graphite is not the direct process, which is involved in the intermediate phase, rhombohedral graphite, when employing the laser ablation method³⁹. Another research reported that the transformation path proceeds through sliding of graphite planes into an unusual orthorhombic stacking⁴⁰. No matter which transformation is, it is only referred to the interconversion between different crystalline structures.

However, coal or coal-derived carbons feature macromolecular structures rather than the lattice structure of graphite. In the chemical structures of coal, there are many weak links between carbon polymeric units, such as aryl structures, as shown in Figure 3a-b. Owing to the weak binding linkages between them, these cross-linking amorphous carbon networks break during laser irradiation in liquid, and the irregular,

polymerized aromatic hydrocarbon units are separated. As the laser ablation process continues, many aromatic fragments will be further broken into smaller amorphous carbon fragments, which sequentially fracture into smaller amorphous carbon particles. Along with these processes, a large amount of aromatic fragments will be released. Then, these aromatic fragments will be further broken into C_2 carbon units during laser ablation in liquid, and their emission signals are captured by a high-resolution spectrograph and an intensified charge coupled device (ICCD). Figure 3g-3h shows the vibration bands in the $\Delta v = 0, -1$ branch of the swan band of C_2 molecules. In the spectra, a clear vibration progression is observed, in which each peak represents a band head of the transition from different initial vibrational quantum states in the upper electronic state⁴¹.

In fact, C_2 dimers do play a key role in the synthesizing diamonds. Zhou *et al.* reported a close relationship between the growth rate of the nanocrystalline diamond film and the concentration of C_2 dimer in the plasma, confirming that C_2 dimer is the growth species of the nanocrystalline diamond⁴². Preliminary works demonstrated the growth of nanocrystalline diamond using C_{60} in microwave discharge, in which strong C_2 swan band optical emission was observed using optical emission spectrometry, and it was proposed that C_2 may be growth species for nanodiamonds⁴³. Based on the analysis above, the C_2 molecule from the laser ablation of coal in liquid should be regarded as the key growth species to transform into nanodiamonds.

The structural stability. Note that there is no obvious size difference among the nanodiamonds synthesized from anthracite, bitumite and coke (approximately 3 nm),

indicating the existence of a common underlying factor. Atomistic models have shown that, for surface bonds terminated with hydrogen atoms and with sizes between 3-5nm, nanometer-sized diamonds are more stable than graphite⁴⁴. In addition, first principles calculations have shown that nanodiamonds of approximately 3nm, and for a broad range of pressures and temperatures, particles with bare, reconstructed surfaces become thermodynamically stable. Preventing larger grain growth means that the surface clusters show a transition from sp^3 carbon to sp^2 carbon⁴⁵. In other words, for the 3-5nm nanodiamonds to achieve stability, the surfaces of the sp^3 clusters must be either stabilized through termination with functional groups or reconstructed into sp^2 carbon. In our case, we do not observe nanodiamonds surrounded by an obvious graphite shell. Therefore, we exclude the hypothesis of a surface transition from sp^3 to sp^2 clusters. However, in our case, the nanodiamonds are functionalized by many hydroxyl and oxygen-containing groups.

In the view of theoretical aspects, Barnard *et al.* have modeled the thermostability of surface functionalization by oxygen, hydroxyl, and water on nanodiamonds⁴⁶. They reported that the oxygen and hydroxyl terminations are thermodynamically favorable and form strong C-O covalent bonds on the nanodiamonds⁴⁶, which is clearly observed at approximately $1000-1200\text{cm}^{-1}$ in our Fourier transform infrared (FTIR) spectrum (Figure 6a). We infer that the role of oxidized functional groups (-COOH and -OH groups) are similar to hydrogen termination, which stabilizes these 3-5nm nanodiamonds.

Generally, oxidized functional groups have the dissimilar properties with the

hydrogen termination. Krueger *et al.* have reviewed recent progress in the surface modification of nanodiamonds⁴⁷, and they pointed out that most of the organic functional groups can be established on the diamond surface, including hydrogen and oxidized groups termination, which prove that nanodiamonds can be stabilized by various groups with different character and not limited to specific one⁴⁷. Therefore, the as-synthesized nanodiamonds with an average size of 3nm and with surfaces modified by many oxidized groups are thermodynamically stable. This conclusion is also strongly supported by the nanodiamonds produced by the detonation technique, which possesses similar size and surface properties⁹.

Based on the experimental observation and the corresponding thermodynamic and kinetic analysis above, the phase transformation path from coal to nanodiamonds *via* C₂ dimer in the process of the laser irradiation in liquid is ascribed as shown in Figure 3i. Under the laser irradiation, these links between the adjacent aromatic units in coal are relatively weak, and will be firstly destroyed by the high energy laser, in this case, and become a large amount of aromatic fragments. Some aromatic fragments will be further broken up into carbon reactive species under the violent bombardment of high energy laser, and the C₂ molecules are dominant. These C₂ dimers form a state of the high temperature, the high pressure and the high density in the plasma region. Based on the thermodynamics analysis on the nucleation of diamond above, the pressure-temperature region of the diamond nucleation is in the range of 10–15 GPa and 4000–5000 K in the carbon phase diagram, exactly coincided with the circumstance provided by laser irradiation³³. Thus, the released C₂ species

subsequently participate in the formation of nanodiamonds as basically structural building blocks. Then, with the plasma quenching, the tiny nanodiamonds with bare surface is very reactive. Thus, the active groups in alcohol rapidly adsorb on their surface. These groups adsorption not only keep nanodiamonds stable, but also provide them with great functionality, such as photoluminescence or readily conjunction with other small molecules.

The photoluminescence spectra of the as-synthesized colloidal nanodiamonds show that the PL emission peak is located at 520 nm when excited at 420 nm (red curve in Figure 5a), and the inset presents a photograph showing bright green fluorescence. The bitumite and coke have stable PL properties (Supplementary Figure S8b and d). The decay times for anthracite, bitumite and coke are 1.84, 0.96 and 1.11 ns, respectively (Supplementary Figure S8a, 8c and 8e). Importantly, no indications of photobleaching are detected for our samples, even after 3 h of continuous excitation with the xenon lamp. The fluorescence spectrum of ablating coal in water has also measured, as shown in the black curve in Figure 5a. Supplementary Figure S9 shows the TEM image, SAED pattern and optical graph of nanodiamonds synthesized in water. From Supplementary Figure S10, we can see that the nanodiamonds synthesized in alcohol and water both show the excitation-dependent luminescence. This phenomenon is identical to the reported fluorescence of nanodiamonds⁴⁸.

Now we turn to explain the fluorescence mechanism of nanodiamonds. It is well known that diamond possess large bandgap of 5.5eV, which make it impossible to emit visible light. So what make it glow? Although the fluorescence mechanism in

nanodiamond colloids was proposed to contain a mixture of sp^2 and sp^3 bonding or radiative recombination due to defect energy-trapping states, the influence of functionalized groups on the fluorescence has not caused enough attention^{48,49}. Recently, we have studied these peculiar phenomena and found that the fluorescence of nanodiamonds possesses two characteristics at least⁵⁰.

First, the excitation-dependent fluorescence. Second, the emission peaks show red shift after heat treatment. In order to judge whether the nanodiamonds synthesized using coal match this criterion, we heat this solution at 65°C. For the sample synthesized in water, the peak shows a significant red shift from 482nm to 502nm and the same situation has also occurred in the samples synthesized in alcohol. Then we use microscopic Fourier transform infrared (MFTIR) spectroscopy to explore detailed information. In detail, the peak located at 1620cm^{-1} is attributed to the bending vibration of OH group⁵¹, while the absorption bands are found to appear in the region of $1650\text{-}1750\text{ cm}^{-1}$, which belong to carbonyl (C=O) groups. Detailed analysis demonstrates that the C=O groups have two categories: ketones C=O and ester C=O groups. The wavenumber of carbonyl IR stretch in an ester is always higher than in a ketone. The stretch peak of $1650\text{-}1685\text{ cm}^{-1}$ always belongs to α,β -unsaturated ketone, while $1730\text{-}1750\text{ cm}^{-1}$ is attributed to C=O stretch of ester groups.^{52,53} From MFTIR spectrum, we can see that OH groups are predominant in the nanodiamonds synthesized in water (black curve in Figure 6b). Very weak ketones C=O groups located at 1675cm^{-1} are also found in the same spectrum. After heating, the ketones C=O groups become stronger (red curve in Figure 6b). For nanodiamonds in alcohol,

OH groups seem weaker than ketones C=O and ester C=O groups (black curve in Figure 6d). After heating at 65°C, ester C=O groups become stronger and dominant in the sample (red curve in Figure 6d). The evolutions of MFTIR spectra demonstrate that oxidation degree become higher, accompanied with the appearance of carbonyl groups as the heating treatment proceed. Therefore, the carbonyl groups, including ketone and ester groups, are probably responsible for the red-shift fluorescence.

Recently, Du *et al.* also found the blue fluorescence in diamond when they dispersed the detonation nanodiamonds in poly(ethylene glycol) solution and employed a microsecond laser ablation⁵⁴. They suggest that ligands on the nanodiamonds surface can significantly improve the visible-light emission and the surface states play a vital role in determining the optical properties. Note that, organic solvents containing C=O and OH groups, such as alcohol and acetic acid, do not give out light. Nevertheless, relying on the nanodiamonds backbone, the formation of some special conformations can be facilitated by the combination of hydroxyl groups and carbonyl groups in the vicinity of the edge of carbon nanomaterials⁵⁰. According to the recent report on graphene oxide, after chemical treatment, local molecular structure can be dominated either by -OH or by the -COOH groups. The -OH-rich GO had an emission peak centered at ~500nm, while the -COOH-rich GO had a broad emission band centered at ~630nm⁵⁵. This proves that the functionalized groups have a key role in the emission wavelength⁵⁶. In other word, the different groups modified nanodiamonds means possessing different bandgaps. Based on the MFTIR spectrum, we infer that the fluorescence color can be simply attributed to three groups

hybridized with nanodiamonds: The OH is blue, ketone C=O is green and ester C=O is yellow. Therefore, the observation can be explained as follows: the original nanodiamonds in water emit blue light due to the dominance of OH groups and then the appearance of ketones C=O lead to the blue-green emission. For alcohol case, the emission peak also exhibit red shift to the yellow region for the reason that the ester C=O groups gradually become stronger. The schematic illustration of effect of various functionalized groups is shown in Figure 6e. In addition, their quantum yields are measured to be 0.06 and 0.035 in alcohol and water, respectively, as shown in Supplementary Figure S11. These results reveal the edges of nanodiamonds can hybridize with neighboring functional groups such as hydroxyl and ketone or ester carbonyl groups to enable emission, which is tunable by modifying surface groups.

4. Conclusion

In summary, we have developed a simple and green approach for synthesizing nanodiamonds from various coals and demonstrated that the unique structure of coal is advantageous for producing nanodiamonds. The synthesized nanodiamonds are monodisperse colloids and exhibit stable and bright green fluorescence in aqueous solution, providing promise for applications in bioimaging engineering, photovoltaics and optoelectronics. The nanodiamonds obtained from coal are significantly smaller than the currently available materials⁹. These particles may facilitate biological applications in which the particle size is critical to transport and drug delivery⁵⁷. These results suggest that coal, which is inexpensive and the most abundant carbon

source material, is useful for the production of nanodiamonds.

Acknowledgments The National Basic Research Program of China (2014CB931700), the National Natural Science Foundation of China (91233203) and the State Key Laboratory of Optoelectronic Materials and Technologies of Sun Yat-sen University supported this work.

References

1. M. Höök, W. Zittel, J. Schindler and K. Aleklett, *Fuel*, 2010, **89**, 3546–3558.
2. P. H. Given, *Fuel*, 1960, **39**, 147–153.
3. M. B. Heredy, L. A. Kostyo and A. E. Neuworth, *Adv. Chem.*, 1966, **55**, 493–502.
4. D. G. Levine, R. H. Schlosberg and B. G. Silbernagel, *P. Natl. Acad. Sci*, 1982, **79**, 3365–3370.
5. N. Berkowitz, *An Introduction to Coal Technology*, 2nd edn, Academic Press, 1993.
6. F. Derbyshire, A. Marzec, H.-R. Schulten, M. A. Wilson, A. Davis, P. Tekely, J.-J. Delpuech, A. Jurkiewicz, C. E. Bronnimann, R. A. Wind, G. E. Maciel, R. Narayan, K. Bartle and C. Snape, *Fuel*, 1989, **68**, 1091–1106.
7. L. Lu, V. Sahajwalla, C. Kong and D. Harris, *Carbon*, 2001, **39**, 1821–1833.
8. V. Singh, D. Joung, L. Zhai, S. Das, S. I. Khondaker and S. Seal, *Prog. Mater. Sci.*, 2011, **56**, 1178–1271.
9. V. N. Mochalin, O. Shenderova, D. Ho, and Y. Gogotsi, *Nature Nanotech.*, 2012, **7**, 11–23.
10. N. R. Greiner, D. S. Phillips, J. D. Johnson, and F. Volk, *Nature*, 1988, **333**, 440–442.
11. G. W. Yang, J. B. Wang and Q. X. Liu, *J. Phys. Condens. Mat.*, 1998, **10**, 7923-7927.
12. M. Frenklach, W. Howard, D. Huang, J. Yuan, K. E. Spear and R. Koba, *Appl. Phys. Lett.*, 1991, **59**, 546-548.
13. S. Welz, Y. Gogotsi and M. J. McNallan, *J. Appl. Phys.*, 2003, **93**, 4207-4214.
14. T. L. Daulton, M. A. Kirk, R. S. Lewis and L. E. Rehn, *Nucl. Instrum. Meth. B*, 2001, **175–177**, 12–20.
15. F. Banhart and P. M. Ajayan, *Nature*, 1996, **382**, 433–435.
16. É. M. Galimov, A. M. Kudin, V. N. Skorobogatskii, V. G. Plotnichenko, O. L.

- Bondarev, B. G. Zarubin, V. V. Strazdovskii, A. S. Aronin, A. V. Fisenko, I. V. Bykov and A. Y. Barinov, *Dokl. Phys.*, 2004, **49**, 150–153.
17. Z. Su, W. Zhou and Y. Zhang, *Chem. Commun.*, 2011, **47**, 4700–4702.
 18. A. Kumar, P. Ann Lin, A. Xue, B. Hao, Y. Khin Yap and R. M. Sankaran, *Nat Commun*, 2013, **4**, 1.
 19. J. Xiao, P. Liu, Y. Liang, H. B. Li and G. W. Yang, *Nanoscale*, 2012, **4**, 7078–7083.
 20. G. W. Yang, *Prog. Mater. Sci.*, 2007, **52**, 648–698.
 21. D. R. Pan and L. S. Kania, *Diamond: electronic properties and applications (Vol. 294)*, Springer, 1994.
 22. A. C. Ferrari and J. Robertson, *Phil. Trans. R. Soc. Lond. A*, 2004, **362**, 2477–2512.
 23. S. Osswald, V. N. Mochalin, M. Havel, G. Yushin and Y. Gogotsi, *Phys. Rev. B*, 2009, **80**, 75419.
 24. P. Mérel, M. Tabbal, M. Chaker, S. Moisa and J. Margot, *Appl. Surf. Sci.*, 1998, **136**, 105–110.
 25. L. Tang, R. Ji, X. Cao, J. Lin, H. Jiang, X. Li, K. S. Teng, C. M. Luk, S. Zeng, J. Hao and S. P. Lau, *ACS Nano*, 2012, **6**, 5102–5110.
 26. J. C. Lascovich, R. Giorgi and S. Scaglione, *Appl. Surf. Sci.*, 1991, **47**, 17–21.
 27. V. Yu. Dolmatov, *Russ. Chem. Rev.*, 2001, **70**, 607–626.
 28. D. M. Shenderova and O. A. Gruen, *Ultrananocrystalline Diamond: Synthesis, Properties, and Applications*, William Andrew, 2006.
 29. S. R. J. Pearce, S. J. Henley, F. Claeysens, P. W. May, K. R. Hallam and J. A. Smith, *Diamond Relat. Mater.*, 2004, **13**, 661–666.
 30. L. Yang, P. W. May, L. Yin, J. A. Smith and K. N. Rosser, *Diamond Relat. Mater.*, 2007, **16**, 725–729.
 31. G. W. Yang, J. B. Wang, C.Y. Zhang and X. L. Zhong, *Chem. Phys. Lett.*, 2002, **361**, 86–90.

32. C. X. Wang, Y. H. Yang, Q. X. Liu, G. W. Yang, Y. L. Mao and X. H. Yan. *Appl. Phys. Lett.*, 2004, **84**, 1471-1473.
33. C. X. Wang, Y. H. Yang and G. W. Yang. *J. Appl. Phys.*, 2005, **97**, 066104.
34. C. X. Wang, Y. H. Yang, N. S. Xu and G. W. Yang, *J. Am. Chem. Soc.*, 2004, **126**, 11303–11306.
35. A. Wilson, *Philos. Mag.*, 1900, **50**, 238.
36. J. B. Wang and G. W. Yang, *J. Phys.: Condens. Matter*, 1999, **11**, 7089-7094.
37. N. V Kozyrev, B. V Larionov and G. V Sakovich, *Combust. Explo. Shock*, 2008, **44**, 193–197.
38. V. V Danilenko, *Combust. Explo. Shock*, 2005, **41**, 577–588.
39. G. W. Yang and J. B. Wang, *Appl. Phys. A*, 2001, **72**, 475-479.
40. S. Scandolo, M. Bernasconi, G. L. Chiarotti, P. Focher and E. Tosatti, *Phys. Rev. Lett.*, 1995, **74**, 4015–4018.
41. T. Sakka, S. Iwanaga, Y. H. Ogata, A. Matsunawa and T. Takemoto, *J. Chem. Phys.*, 2000, **112**, 8645-8653.
42. D. Zhou, D. M. Gruen, L. C. Qin, T. G. McCauley and A. R. Krauss, *J. Appl. Phys.*, 1998, **84**, 1981-1989.
43. D. M. Gruen, S. Liu, A. R. Krauss and X. Pan, *J. Appl. Phys.*, 1994, **75**, 1758-1763.
44. P. Badziag, W. S. Verwoerd, W. P. Ellis and N. R. Greiner, *Nature*, 1990, **343**, 244–245.
45. J.-Y. Raty and G. Galli, *Nature Mater.*, 2003, **2**, 792–795.
46. L. Lai and A. S. Barnard, *Nanoscale*, 2011, **3**, 2566–2575.
47. A. Krueger and D. Lang, *Adv. Funct. Mater.*, 2012, **22**, 890–906.
48. D. Tan, S. Zhou, B. Xu, P. Chen, Y. Shimotsuma, K. Miura, and J. Qiu, *Carbon*, 2013, **62**, 374–381.
49. S. Hu, S. Guo, Y. Dong, Y. Yang, J. Liu and J. Cao, *J. Mater. Chem.*, 2012, **22**,

12053-12057.

50. J. Xiao, P. Liu, L. Li and G. W. Yang, *J. Phys. Chem. C.*, 2015, **119**, 2239–2248.
51. Y. Yang, C. Liu, P. Mao and L. J. Wang, *J. Nanomaterials*, 2013, **2013**, 13:13–13:13.
52. K. Nakanishi and P. H. Solomon, *Infrared absorption spectroscopy*, Lolden-Day, San Francisco, 1977.
53. R. Silverstein and F. Webster, *Spectrometric identification of organic compounds*, John Wiley & Sons, 2006.
54. K. Y. Niu, H. M. Zheng, Z. Q. Li, J. Yang, J. Sun and X. W. Du, *Angew. Chem. Int. Ed.*, 2011, **50**, 4099–4102.
55. S. K. Cushing, M. Li, F. Huang and N. Wu, *ACS Nano*, 2014, **8**, 1002–1013.
56. X. Li, S. Zhang, S. A. Kulinich, Y. Liu and H. Zeng, *Sci. Rep.*, 2014, **4**, 4976.
57. E. K. Chow, X. Q. Zhang, M. Chen, R. Lam, E. Robinson, H. Huang, D. Schaffer, E. Osawa, A. Gog and D. Ho, *Sci. Trans. Med.*, 2011, **3**, 73ra21–73ra21.

Table 1. Summary of peak positions and area for fitting XPS.

	Raw coal			Nanodiamonds		
	Position(eV)	Area	FWHM(eV)	Position(eV)	Area	FWHM(eV)
sp ³	285.000	7339.962	1.883	285.000	20255.130	1.312
sp ²	284.312	20219.50	0.791	284.300	2748.710	0.860
C-O	-	-	-	286.487	11615.2	2.158
C=O	-	-	-	288.731	2583.24	1.505

Figure Captions

Figure 1. Nanodiamonds from raw anthracite coal. (a) Macroscopic images of raw anthracite. (b) SEM image of ground anthracite coal with a broad size distribution ranging from several to hundreds of microns in diameter; the inset presents the corresponding EDS spectrum, which shows that anthracite coal contains pure carbon without impurities. (c) A low-magnification image of the as-synthesized nanodiamonds and their size distributions (the inset), which indicates that the nanodiamonds are unagglomerated and uniformly sized. (d) SAED pattern shows the typical three strong diffraction rings of diamond. (e) EDS spectrum of the nanodiamonds. The O and Cu elements originate from the C=O functional groups and the copper grid, respectively. (f-h) HRTEM images of the various structures of the nanodiamonds, including monocrystalline and twinning structures.

Figure 2. Structures of anthracite and nanodiamonds. (a) XRD pattern of anthracite coal (black line) that shows no diffraction ring but rather a hump near 26° , indicating an amorphous material. The XRD pattern of the nanodiamonds (red line) shows a diffraction peak at 44° , which is in agreement with the (111) plane of cubic diamond. (b) Ultraviolet micro-Raman spectra of anthracite coal (black line) and nanodiamonds (red line). The peak at 1382 cm^{-1} exhibits an obvious downshift to approximately 1325 cm^{-1} from coal to nanodiamonds and becomes narrower, which is consistent with the phonon-confined scattering of small nanodiamonds (3.1nm). (c) High-resolution C1s XPS spectra of anthracite coal (black squares) and nanodiamonds

(red squares). The main feature of coal is located at 284.3eV, which corresponds to sp^2 carbon. However, the nanodiamonds peak shifts to 285eV, which corresponds to sp^3 carbon.

Figure 3. Capturing intermediate phase in the transition from coal to nanodiamonds. (a-b) Intersecting and overlapping amorphous carbon network forms after the laser irradiation of coal (taken from the 5th bottle in Supplementary Figure S6) (c-d) The network fractures into small pieces, similar to the shape of a necklace (taken from the 7th bottle in Supplementary Figure S6). (e-f) The small fragments break into many amorphous carbon particles (taken from the 8th bottle in Supplementary Figure S6). (g-h) The spectrum of the resolved C_2 Swan band emission for $\Delta v = 0, -1$, respectively. (i) Schematic representations of the process of transformation from coal into nanodiamonds.

Figure 4. Nucleation thermodynamics of nanodiamonds. (a) The relationship between the nanosize-induced additional pressure and nuclei size. (b) The dependence of nucleation radius r of nanodiamonds on the pressure. (c) The relationship between critical energy and pressure under the various temperatures. (d) The probability of phase transition upon LAL under the condition that $r=3\text{nm}$.

Figure 5. PL spectrum of nanodiamonds. (a) PL emission of nanodiamonds synthesized in water (black line) and alcohol (red line) excited at 420 nm, and the

inset shows the bright green and blue fluorescence of colloid nanodiamonds synthesized in alcohol and water, respectively. (b) The time-resolved photoluminescence decay profiles of nanodiamonds synthesized in alcohol, and the inset shows the photostability of nanodiamonds with a 450 W xenon lamp under 3 h of irradiation; no photobleaching was observed.

Figure 6. The fluorescence mechanism of nanodiamonds. (a-b) The fluorescence of nanodiamonds synthesized in water before and after heating at 65°C and corresponding MFTIR spectrum showing the increase of ketones C=O groups. (c-d) The fluorescence of nanodiamonds synthesized in alcohol before and after heating at 65°C and corresponding MFTIR spectrum showing the increase of ester C=O groups. (e) The schematic illustration of effect of various hybridized groups.

Figure 1

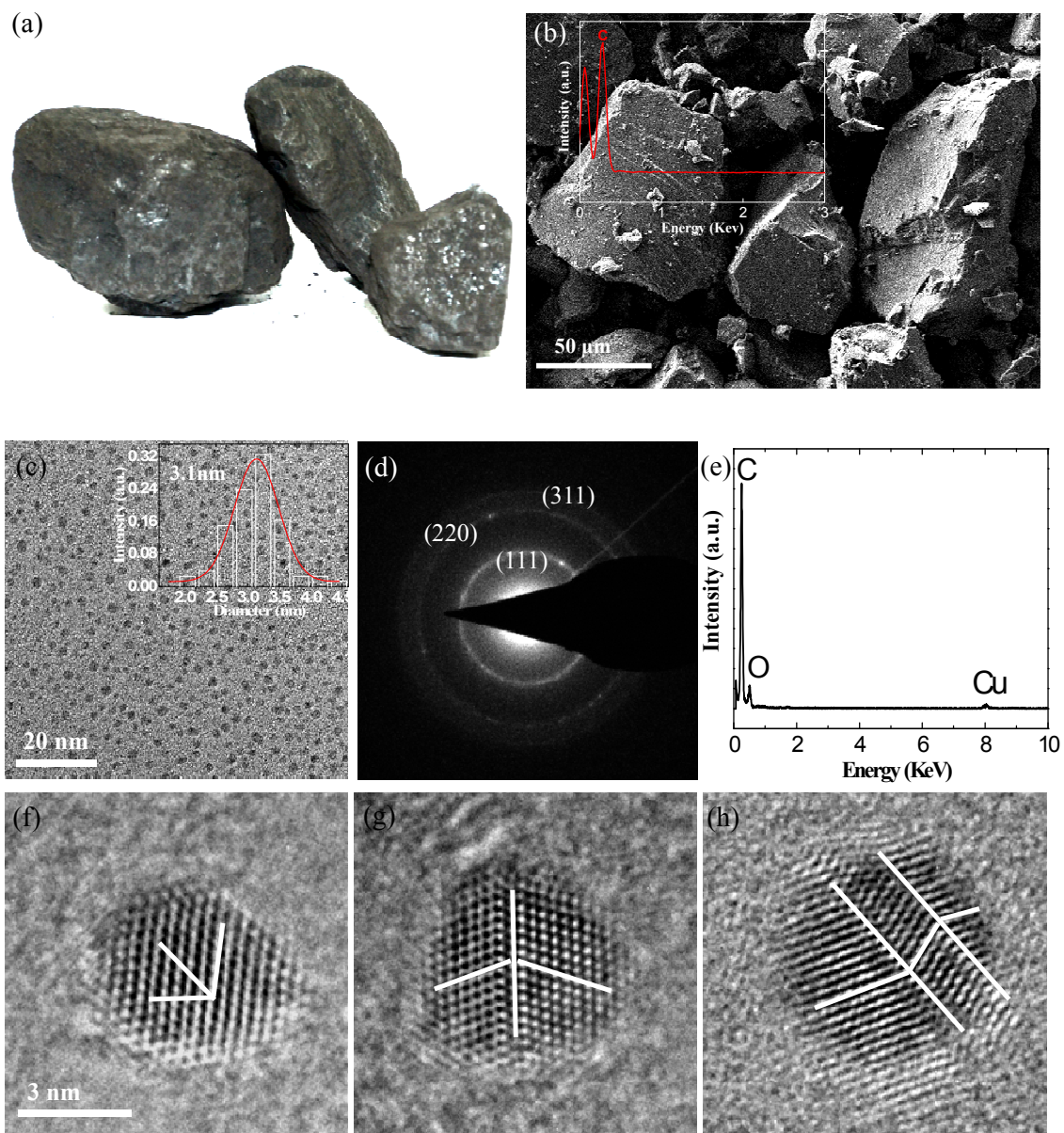


Figure 2

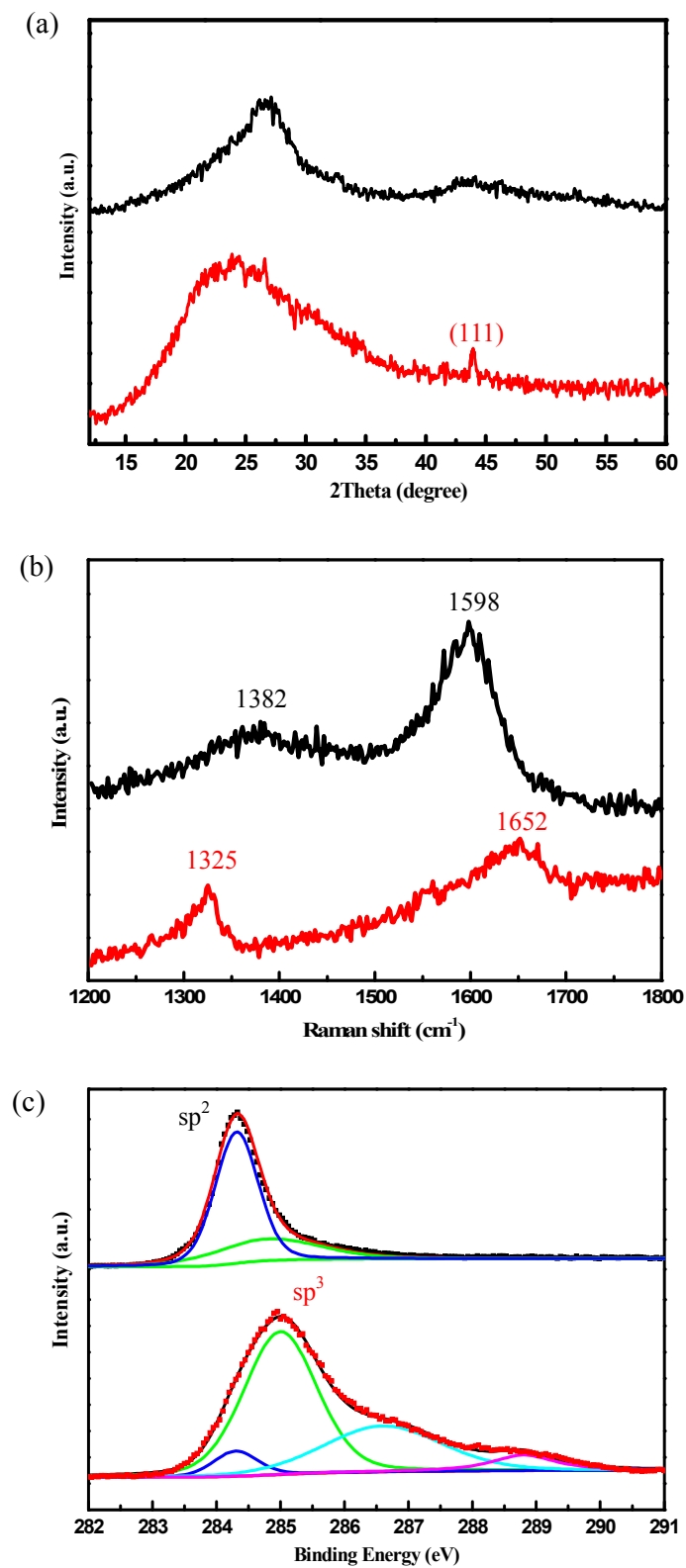


Figure 3

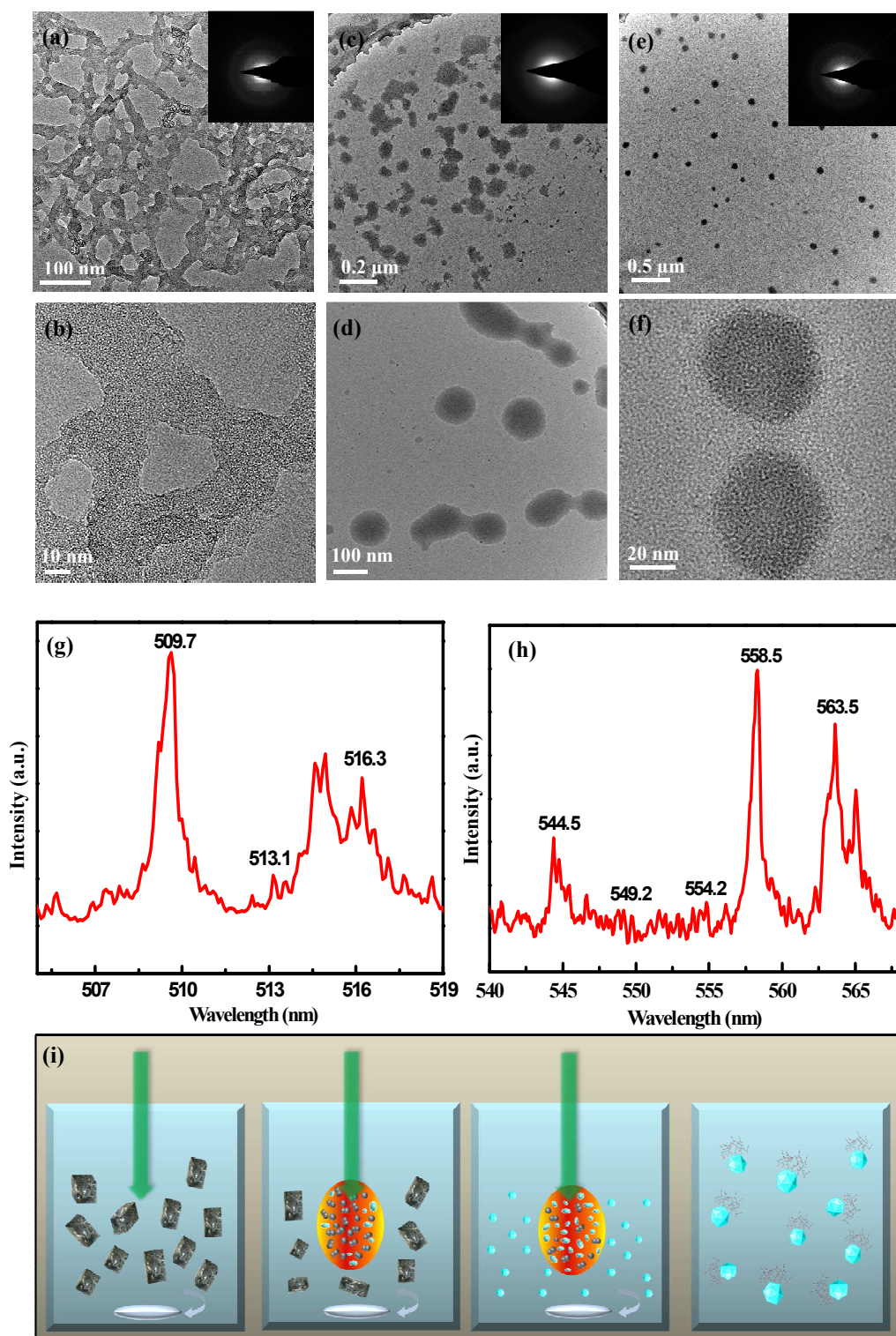


Figure 4

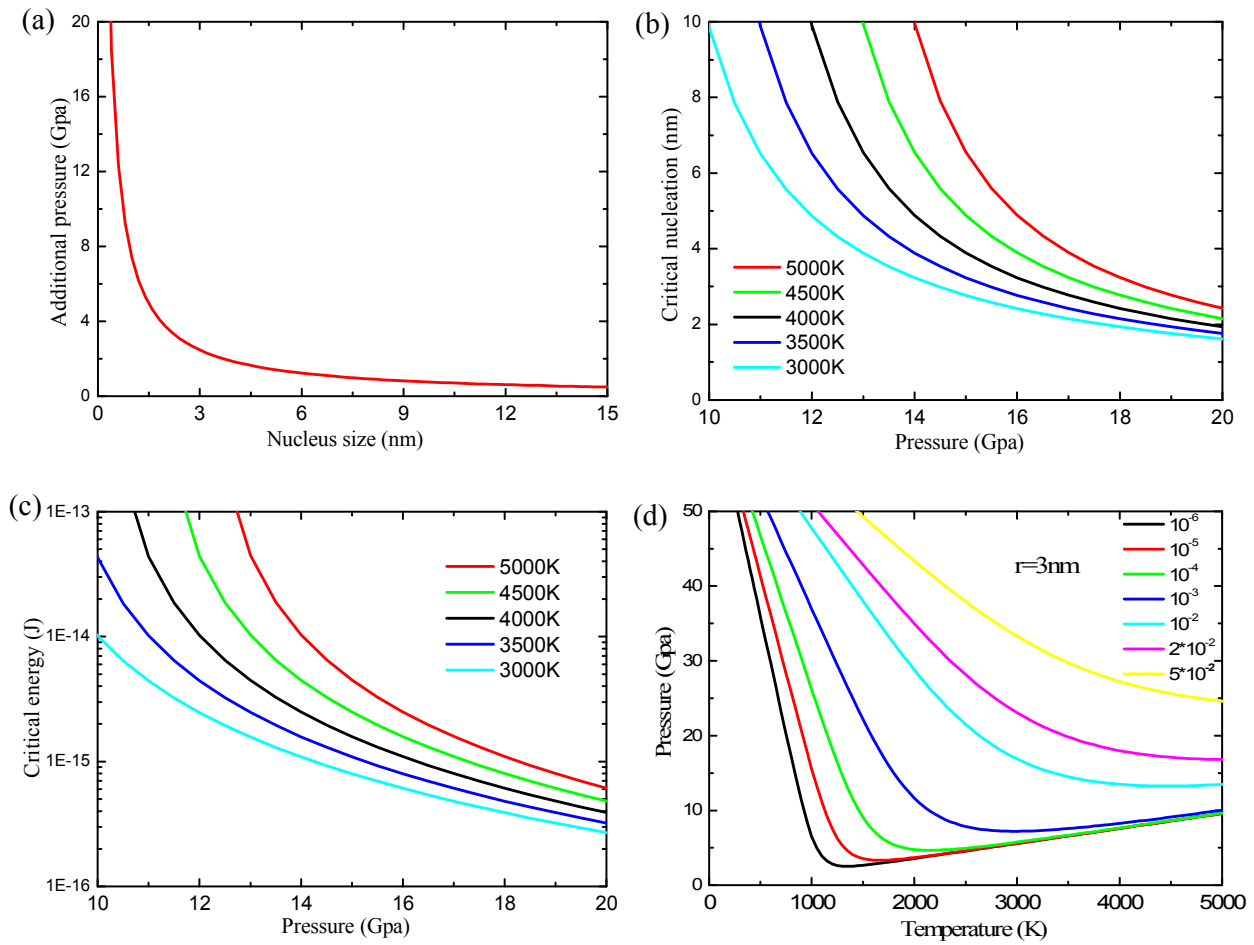


Figure 5

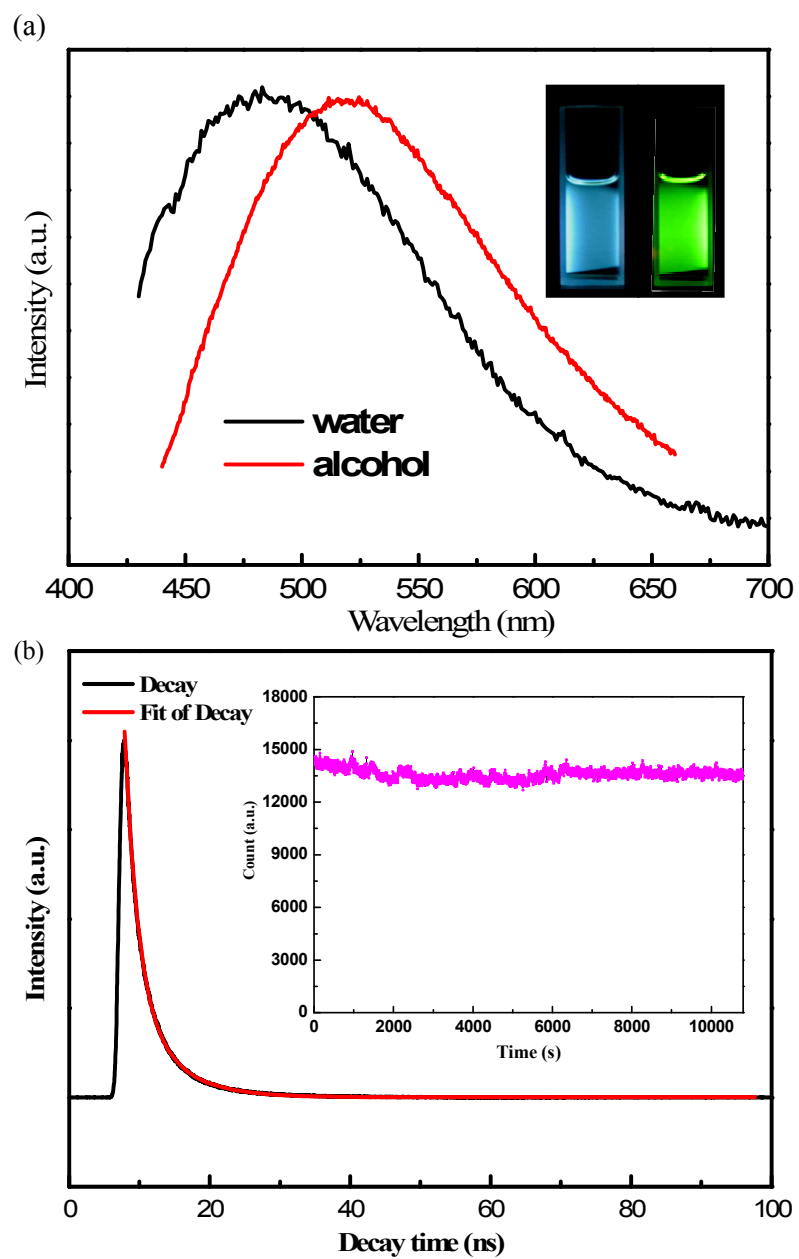


Figure 6

